This article has been accepted for inclusion in a future issue of this journal. Content is final as presented, with the exception of pagination.



# State-of-Grid-Based SoC Balancing and AC Coupling Control for DC Microgrids

Ömer Ekin, *Graduate Student Member, IEEE*, Max Leuthaeusser, *Student Member, IEEE*, Giovanni De Carne, *Senior Member, IEEE*, and Veit Hagenmeyer, *Member, IEEE*

***Abstract*—The shift towards renewable energy has increased interest in dc microgrids as a promising integration solution. However, managing power-sharing, state-of-charge (SoC) balancing, and reliable ac coupling without communication remains challenging, necessitating advanced control methods. This article introduces a novel state-of-grid-based control for dc microgrids, enabling communication-free power-sharing and SoC balancing across battery systems, even with significant line resistances, while supporting synergistic ac coupling. Each battery locally projects its SoC into a small voltage offset around the nominal dc bus level; the resulting bus voltage therefore mirrors the average SoC of the entire microgrid. By using an analogous mapping for ac frequency, a single voltage–frequency metric unifies dc and ac domains. A small-signal Lyapunov analysis proves local exponential stability under realistic parameter spreads. The controller is implemented on a laboratory microgrid comprising two battery emulators, photovoltaic generation, programmable loads, and a Silicon Carbide interlink converter. Hardware results in islanded and grid-connected modes confirm voltage regulation, SoC equalization, and seamless power exchange.**

***Index Terms*—Battery energy storage system (BESS), dc microgrid, decentralized control, power management, SoC-balancing, state-of-grid (SoG).**

## Nomenclature

| | |
|---|---|
| $V_{\mathrm{dc}}$ | DC bus Voltage [V]. |
| $V_{\mathrm{dc}}^{*}$ | Reference dc bus voltage [V]. |
| $V_{\mathrm{C,B}i}$ | Converter Output Voltage of $i^{\mathrm{th}}$ battery [V]. |
| $\kappa_i$ | SoC-dependent scaling factor for $V_{\mathrm{C,B}i}$ [-]. |
| $\sigma$ | Globally defined mapping gain [-]. |
| $\mathrm{SoC}_i$ | State-of-Charge of $i^{\mathrm{th}}$ battery (0 . . . 1) [-]. |
| $\mathrm{SoC}_i^{*}$ | Desired State-of-Charge of $i^{\mathrm{th}}$ battery [-]. |
| $\mathrm{SoC}_{\Delta,i}$ | Correction factor in the SoC mapping [-]. |
| $\mathrm{SoG}_{\mathrm{dc},i}$ | SoG index of $i^{\mathrm{th}}$ dc microgrid [-]. |
| $\mathrm{SoG}_{\mathrm{ac},j}$ | SoG index of $j^{\mathrm{th}}$ ac microgrid [-]. |
| $f_{\mathrm{ac}}$ | Measured grid frequency [Hz]. |
| $f_{\mathrm{ac}}^{*}$ | Reference grid frequency [Hz]. |
| $P_{ij}^{*}$ | Active power transferred by the VSC between $i^{\mathrm{th}}$ dc microgrid and $j^{\mathrm{th}}$ ac microgrid [W]. |
| $P_{\mathrm{VSC}}^{\max}$ | Rated active power of the VSC [W]$P_{\mathrm{VSC}}^{\min}$ VSC dead-band limit [W]. |
| $I_{\mathrm{VSC}}$ | DC current of the interlink converter [A]. |
| $C_{\mathrm{dc}}$ | DC-link capacitance [F]. |
| $C_i$ | Capacity of $i^{\mathrm{th}}$ battery [Ah]. |
| $R'_{\mathrm{B}i}$ | Line/internal resistance of $i^{\mathrm{th}}$ battery [Ω]. |

Received 2 July 2025; revised 9 September 2025 and 14 October 2025; accepted 20 November 2025. This work was supported in part by Helmholtz Association under the program “Energy System Design” and Helmholtz Young Investigator Group “Hybrid Networks” under Grant VH-NG-1613. *(Corresponding author: Ömer Ekin.)*

Ömer Ekin, Max Leuthaeusser, and Veit Hagenmeyer are with the Institute for Automation and Applied Informatics (IAI), Karlsruhe Institute of Technology (KIT), 76131 Karlsruhe, Germany (e-mail: oemer.ekin@kit.edu).

Giovanni De Carne is with the Institute for Technical Physics (ITEP), Karlsruhe Institute of Technology (KIT), 76131 Karlsruhe, Germany.

Digital Object Identifier 10.1109/TIE.2025.3639739

## I. Introduction

THE increasing integration of renewable energy sources (RES), electric vehicles, and decentralized energy storage systems calls for a paradigm shift in power distribution. Direct current (dc) microgrids have emerged as a suitable architecture for integrating these components, offering advantages such as fewer conversion stages, reduced semiconductor usage, higher efficiency, and improved compatibility with inherently dc-native technologies [1], [2]. Their modular nature and absence of frequency synchronization requirements make them particularly suitable for distributed generation, industrial automation, and commercial buildings [3], [4].

The dc microgrid architecture considered in the present work, depicted in Fig. 1, comprises two battery energy storage systems (BESSs), a 6 kWp photovoltaic (PV) string, resistive loads at 120 V and 230 V, and an ac interlink converter (IC) compliant with the ride-through and islanding requirements defined in IEEE Std 1547-2018 [5]. This topology reflects typical communication-sparse rural or behind-the-meter installations.

While the primary control objective of dc microgrids is to regulate the bus voltage within a desired range, other essential control objectives are indispensable for the implementation of practical dc microgrids. These include power-sharing capabilities, state-of-charge (SoC) balancing, and the provision of ancillary services between the dc microgrid and an ac grid [6], [7].

© 2026 The Authors. This work is licensed under a Creative Commons Attribution 4.0 License. For more information, see https://creativecommons.org/licenses/by/4.0/

This article has been accepted for inclusion in a future issue of this journal. Content is final as presented, with the exception of pagination.



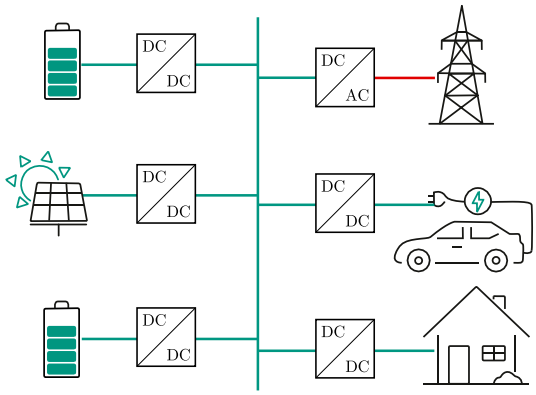


Fig. 1. Schematic block diagram of the laboratory dc microgrid used in this study (two BESS, 6 kWp PV, resistive loads, and ac interlink).

SoC balancing is critical for maintaining the stability of dc microgrids. Without proper balancing, some batteries may become fully charged or fully discharged prematurely. In both cases, the collective ability of the storage system to absorb or supply power is reduced, which can lead to instability, especially during periods of surplus or deficit in renewable generation. Moreover, operating batteries outside their optimal SoC range accelerates degradation, reducing their lifespan and the overall reliability of the system. Effective SoC balancing therefore plays a key role in enhancing efficiency, extending battery life, and ensuring stable and resilient grid operation [8], [9].

In hierarchical control-based approaches, high-frequency communication is required for steady and dynamic power-sharing capability [10]. Such a communication requirement in an energy grid increases complexity and costs. In addition, communication technology introduces challenges such as vulnerability to cyber-attacks, reliability concerns, compatibility issues, privacy and data security risks, regulatory compliance requirements, maintenance challenges, and dependency on external networks [11]. Decentralized approaches operate based on measurements available locally to each component, thereby avoiding the drawbacks of communication-based methods. For instance, droop based-control can achieve power-sharing capability without communication, however, it involves an inherent trade-off between voltage regulation and load-sharing accuracy [12].

Various approaches have been proposed to improve SoC balancing and decentralized control in dc microgrids. These can be broadly grouped into: 1) SoC-driven local adaption; 2) adaptive droop-based control; and 3) hybrid ac/dc coordination.

In [13], an adaptive droop strategy is combined with an online capacity estimation via the Salp swarm algorithm (SSA), enabling proportional power-sharing according to the actual available capacity of each battery. While this method accounts for ageing effects, it remains confined to the dc side, has only been demonstrated in simulation, and does not address ac coupling or experimental validation.

In [14], an SoC-dependent sigmoid-shaped droop is combined with virtual voltage-drop equalization to mitigate feeder-impedance mismatch and bus-voltage compensation for voltage restoration; low-bandwidth neighbor exchange is employed for distributed averaging, and the method demonstrates fast SoC equalization and accurate current sharing in simulation and HIL with a supporting stability analysis. However, it still relies on communication and does not address ac-side coordination.

In [15], an exponentially SoC-scaled droop is augmented by a current-offset compensation term to explicitly counteract feeder-impedance mismatch, complemented by PI-based bus-voltage restoration; the approach is validated analytically, in simulation, and experimentally, yet it requires low-bandwidth communication and remains confined to dc-side control.

SoC-scaling approaches [16], [17] adjust power setpoints based on SoC levels but assume equal battery capacities and neglect the charging process in early works. More recent methods such as adaptive SoC-based droop [18] allow for heterogeneity but have only been validated in simulation. Reference-voltage-based SoC balancing methods such as [19] operate without communication, yet do not consider ac-side integration. The approach in [20] uses droop coefficient adaptation to achieve SoC balancing in islanded dc microgrids, but lacks grid coupling.

Other methods [21] rely on network-wide data exchange, which limits scalability. Hybrid ac/dc approaches such as [22] normalize ac frequency and dc voltage to enable intergrid power-sharing but enforce near-continuous interlink operation, leading to increased converter losses. The work in [23] introduces energy-storage-based smoothing but lacks SoC coordination. Distributed control of ICs is explored in [24], while [25] and [26] propose control via SoC-reflective voltages or ac signal injection.

In [28], a SoC-based droop regulates the dc bus: the voltage reference is held constant within a nominal SoC range and adjusted only at low or high SoC to limit bus variation; the droop gain adapts with SoC for balancing, and PV/utility coordination relies on dc bus signaling with predefined thresholds. The approach is restricted to dc side balancing and has not been demonstrated in real hardware experiments.

In summary, existing schemes predominantly address either dc-side SoC equalization or the interlink converter in isolation; a unified strategy that realizes dc–ac cross-domain SoC balancing while explicitly accounting for heterogeneous batteries and realistic feeder resistances has not yet been reported. Table I summarizes these approaches based on the literature review. Synergistic ac coupling refers to a bidirectional grid supportive functionality of the IC. Check marks in brackets indicate that certain criteria are partially fulfilled. For instance, hardware (HW) experiments conducted at limited power levels or using hardware-in-the-loop (HIL) setups are viewed as a preliminary step, yet may not fully meet the requirements for real HW applications.

In the present article, the term state-of-grid (SoG) is introduced and used as a unifying metric that encodes the system-level energy state in measurable bus variables. Each converter maps its local SoC to a small deviation of the common dc bus voltage reference and, via frequency normalization, to an equivalent deviation of the ac frequency reference. The resulting bus variables act as a self-organizing field that conveys the global energy state to every node, enabling them

This article has been accepted for inclusion in a future issue of this journal. Content is final as presented, with the exception of pagination.



TABLE I
STATE-OF-THE-ART COMPARISON

| References | Focus | Communication Free | SoC-Balancing | Synergistic ac-Coupling | HW Validated |
|---|---|---|---|---|---|
| [13] | Adaptive droop with capacity estimation (SSA) | ✓ | ✓ | × | × |
| [14] | LBC / distributed estimation | (✓) | ✓ | × | (✓) |
| [15] | Exponential SoC-scaled droop | (✓) | ✓ | × | ✓ |
| [16], [17] | SoC based droop | ✓ | ✓ | × | ✓ |
| [18] | SoC based droop | ✓ | ✓ | × | × |
| [19] | DC bus voltage signaling | ✓ | ✓ | × | ✓ |
| [20] | Adaptive droop | ✓ | ✓ | × | ✓ |
| [21] | Virtual power rating | (✓) | ✓ | × | ✓ |
| [22], [23] | Normalized droop ac-dc interlink | ✓ | × | ✓ | ✓ |
| [24] | Normalized droop ac-dc interlink | ✓ | × | ✓ | ✓ |
| [25] | SoC based Voltage | ✓ | ✓ | × | × |
| [26] | AC superimposed on dc voltage to modify droop | ✓ | × | ✓ | ✓ |
| [27] | Filter based Decentralized Control | ✓ | ✓ | × | (✓) |
| [28] | Master/Slave bus voltage | ✓ | ✓ | (✓) | (✓) |
| The present paper | Flexible dc voltage SoG based control | ✓ | ✓ | ✓ | ✓ |

to adjust their power set-points autonomously. Consequently, the microgrid: 1) balances SoC across heterogeneous battery energy-storage systems (BESSs); 2) shares power robustly under realistic feeder resistances and capacity spread; and 3) exchanges power with the utility grid through an IC, without any required communication link. The concept is validated on a hardware testbed in both islanded and grid-connected modes, considering various scenarios of line impedance and load variations.

### A. Summary of Contributions

The key contributions of this article are as follows.

1) Introduction of the SoG metric, which unifies SoC, voltage, and frequency to enable fully decentralized, communication-free control.
2) A novel control scheme that enables.
   i) Effective SoC balancing across dc and ac coupled BESS units.
   ii) Synergistic dc–ac coupling, where the interlink converter supports both grids autonomously.
   iii) Robust power-sharing, resilient to line resistance and capacity variations.
   iv) An inherent tertiary interface via SoG reference adjustment for system-level optimization.

The proposed framework is validated through a comprehensive analytical and experimental evaluation. The analysis includes a Lyapunov-based small-signal stability proof and an input-to-state stability (ISS) assessment under ac-side disturbances. Experimental validation is conducted in a dc microgrid setup, demonstrating the effectiveness of the approach under islanded and grid-connected operation with realistic feeder resistances, line impedances, and varying load conditions.

The remainder of this article is structured as follows. The proposed control strategy is explained in Section II. In Section III the dc microgrid configuration and components are explained. Section IV provides the stability proof for the method. In Section V, the performance of the proposed control strategy is demonstrated through a dc microgrid experimental setup. Finally, a conclusion is given in Section VI.

## II. PROPOSED SOG-BASED CONTROL METHOD

This section formalizes the SoG concept obtained by merging the SoC-driven bus-voltage control of Section II-A with the SoG-based interlink-converter (IC) strategy of Section II-B, hereafter referred to as SoG-based control. Each energy-storage system (ESS) interfaces with the common dc bus through a dedicated dc/dc-converter, as illustrated in Fig. 1. The key idea is that if several converters attempt to impose slightly different output voltages within a narrow operational band around the nominal dc bus voltage, the resulting power exchange naturally reflects each unit's SoC. Due to the parallel connection and voltage-based control, the actual dc bus voltage emerges as a weighted average of the individual converter setpoints. As such, it implicitly encodes the aggregate energy state of all ESS units into a single physical quantity-the bus voltage-allowing it to be interpreted as the SoG. At the IC, the same deviation is mapped to an equivalent frequency offset, providing a unified coordination signal to both dc- and ac-side converters. Unlike in conventional ac grids, in which frequency drifts passively in response to instantaneous generation-load imbalance, the proposed microgrid modulates bus voltage (and its frequency analogue) actively around nominal values to encode the longer-term energy balance of the storage fleet. Positive excursions indicate an SoC surplus, whereas negative excursions denote reduced reserves. The SoG thus offers every converter a real-time, communication-free estimate of the overall energy availability in the system, enabling decentralized power-sharing actions while preserving tight voltage and frequency regulation.

*Remark:* In the present article, the ac grid is assumed to have a predominantly inductive behavior. For ac grids with resistive characteristics, the approach can be adapted using the voltage-based SoG mapping on the ac side to control the active power. Unless otherwise stated, the nominal references used throughout this article are $V_{\mathrm{dc}}^{*} = 700\,\mathrm{V}$ and $f_{\mathrm{ac}}^{*} = 50\,\mathrm{Hz}$. For the ac side, we assume a three-phase system with $V_{\mathrm{ac,L2L}}^{*} = 400\,\mathrm{V}$ (line-to-line RMS).

This makes it possible to control the IC in such a way that it regulates a relative deviation between the SoGs. This ensures that the dc microgrid and the ac grid will be controlled to

This article has been accepted for inclusion in a future issue of this journal. Content is final as presented, with the exception of pagination.



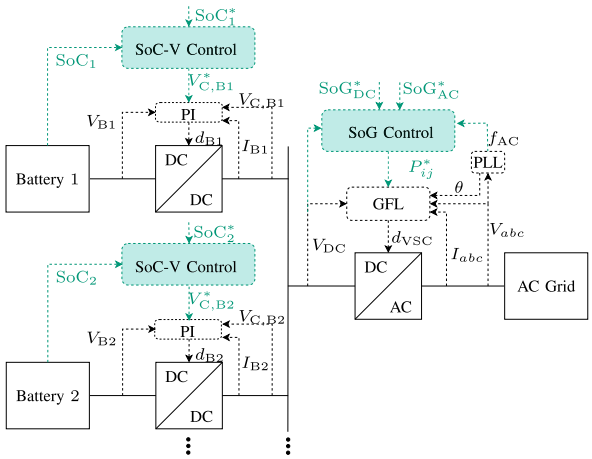


Fig. 2. Proposed decentralized microgrid control scheme.

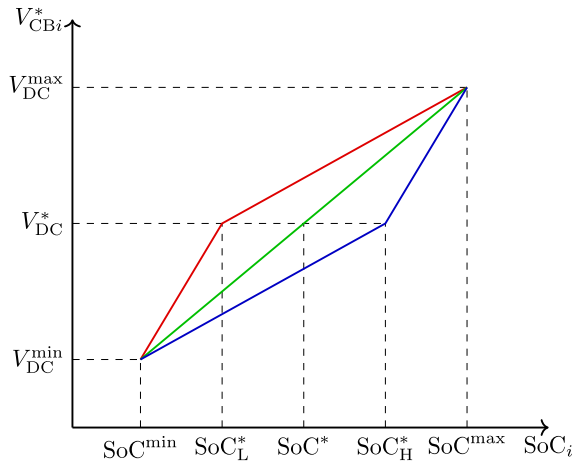


Fig. 3. Voltage–SoC mapping for three exemplary SoC setpoints derived from (1)–(3). the plot illustrates three cases: 1) low setpoint $\mathrm{SoC}_{\mathrm{L}}^*$ near $\mathrm{SoC}^{\min}$ (red line); 2) high setpoint $\mathrm{SoC}_{\mathrm{H}}^*$ near $\mathrm{SoC}^{\max}$ (blue line); and 3) centered setpoint $\mathrm{SoC}^*$ (green line). The correction factor $\mathrm{SoC}_{\Delta,i}$ ensures that the slope of the voltage reference mapping is adjusted to maintain symmetric sensitivity to deviations around each setpoint.

maintain the same state. The control scheme is depicted exemplary for some key components in Fig. 2. The SoC-based method controls the output voltages of each battery's dc/dc converter in the dc microgrid according to its SoC. With the converters connected in parallel to the dc bus, a higher voltage setpoint at any converter causes current (and thus power) to flow towards the grid. Conversely, a lower voltage setpoint than the bus voltage causes current to flow toward the battery. This control method naturally balances SoC across the batteries in the dc microgrid.

### A. Proposed SoC-V Based Control

The proposed SoC-V control is implemented using

$$V_{\mathrm{C,B}i}^* = V_{\mathrm{dc}}^* \cdot \kappa_i \tag{1}$$

$$\kappa_i = 1 + \sigma \frac{\mathrm{SoC}_i - \mathrm{SoC}_i^*}{\mathrm{SoC}_{\Delta,i}} \tag{2}$$

where $V_{\mathrm{C,B}i}^*$ is the controlled output voltage of the converter of battery $i \in \mathbb{N}^+$ and $\kappa_i \in [\kappa_{\min}, \kappa_{\max}]$ is a scaling factor based on the respective SoC, and $\sigma \in [0,1]$ represents the globally defined permissible deviation across all grids. To guarantee proper ac-side operation, the dc bus voltage must remain above $\sqrt{2}V_{l,\mathrm{rms}} \approx 565.7\,\mathrm{V}$, where $V_{l,\mathrm{rms}}$ denotes the line-to-line RMS voltage of the three-phase ac system. With a 10% margin, this results in a minimum requirement of $V_{\mathrm{dc}}^{\min} \geq 622.25\,\mathrm{V}$. Since the SoG mapping allows relative deviations of $\pm\sigma$ around the nominal reference $V_{\mathrm{dc}}^*$, $\sigma$ must satisfy

$$\sigma < 1 - \frac{V_{\mathrm{dc}}^{\min}}{V_{\mathrm{dc}}^*}. \tag{3}$$

This condition ensures that the dc bus voltage remains within the admissible range even under maximum negative deviation. Unlike traditional control approaches that aim to restore bus voltage and ac frequency strictly to their nominal values, the proposed method intentionally allows a limited deviation ($\pm\sigma$), which is used as an implicit coordination signal. This deviation remains small (e.g., $\pm 5\,\%$) and does not compromise operational stability, as shown in Section IV. In the present article, $\sigma$ is set to 0.05, representing a permissible deviation of 5 % in the dc bus voltage. $\mathrm{SoC}_i, \mathrm{SoC}_i^* \in [0,1]$ are the measured and the desired SoC of $i^{\text{th}}$ battery. The $\mathrm{SoC}_{\Delta,i}$ is a correction factor and defined as

$$\mathrm{SoC}_{\Delta,i} = \begin{cases} \mathrm{SoC}_i^{\max} - \mathrm{SoC}_i^*, & \text{if } \mathrm{SoC}_i - \mathrm{SoC}_i^* > 0 \\ \mathrm{SoC}_i^* - \mathrm{SoC}_i^{\min}, & \text{otherwise} \end{cases} \tag{4}$$

where $\mathrm{SoC}_{\Delta,i} \neq 0$, $\mathrm{SoC}_i^{\min}$, $\mathrm{SoC}_i^{\max}$, and $\mathrm{SoC}_i^*$ denote the minimum, maximum, and desired SoC for $i^{\text{th}}$ battery, respectively. The purpose of the case differentiation in (4) is to normalize the influence of SoC deviations depending on the position of the setpoint $\mathrm{SoC}_i^*$ within the SoC range. This ensures that the scaling factor $\kappa_i$ from (1) produces an appropriate voltage adjustment—symmetrical in effect relative to the SoC deviation—even when the setpoint is asymmetrically located. As illustrated in Fig. 3, three scenarios are shown: a low setpoint $\mathrm{SoC}_{\mathrm{L}}^*$ near $\mathrm{SoC}_i^{\min}$ (red), a high setpoint $\mathrm{SoC}_{\mathrm{H}}^*$ near $\mathrm{SoC}_i^{\max}$ (blue), and a centered setpoint $\mathrm{SoC}^*$ (green). Without the correction term $\mathrm{SoC}_{\Delta,i}$, the slope of the voltage mapping would be constant and lead to uneven sensitivity: SoC deviations in one direction would have a stronger impact than in the other. By adapting the slope dynamically through $\mathrm{SoC}_{\Delta,i}$, the controller ensures that reactions to SoC deviations are scaled appropriately regardless of where $\mathrm{SoC}_i^*$ lies. By applying the mapping (1)–(4), an inherent SoC balancing is achieved. Interfacing with the system is possible through the $\mathrm{SoC}^*$ and $\mathrm{SoG}^*$ reference values, allowing tertiary control to enhance functionality. However, tertiary control is not required for the core operation of the method, which remains fully functional without it.

### B. Proposed SoG-Based DC–AC Interlink Control

The control method proposed in the present work for regulating the dc-ac IC is based on inverse mapping of (1)–(4), for which we introduce the following definition.

*Definition 1 (SoG):* The SoG is chosen as a representative quantity for dc and ac microgrids gained through a

This article has been accepted for inclusion in a future issue of this journal. Content is final as presented, with the exception of pagination.



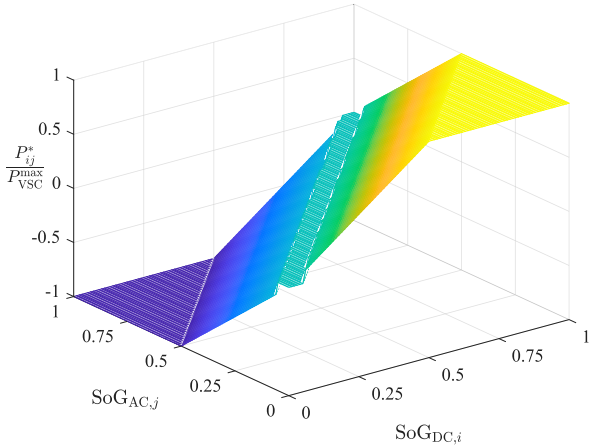


Fig. 4. Exemplary plot of $P^*_{ij}$ with $\text{SoG}^*_{\text{dc},i} = \text{SoG}^*_{\text{ac},j} = 0.5$ and $\sigma = 0.05$.

feature-normalized mapping between the two physical quantities. For dc microgrids the SoG is defined as

$$\text{SoG}_{\text{dc},i} = \text{SoG}^*_{\text{dc},i} + \frac{\text{SoG}_{\Delta,i}}{\sigma} \cdot \left( \frac{V_{\text{dc},i}}{V^*_{\text{dc}}} - 1 \right) \tag{5}$$

and for ac microgrids with

$$\text{SoG}_{\text{ac},j} = \text{SoG}^*_{\text{ac},j} + \frac{\text{SoG}_{\Delta,j}}{\sigma} \cdot \left( \frac{f_{\text{ac},j}}{f^*_{\text{ac}}} - 1 \right) \tag{6}$$

with $\text{SoG}^*_{\text{dc},i}, \text{SoG}^*_{\text{ac},j}$ being the desired dc and ac SoG references for the $i^{\text{th}}$ dc and $j^{\text{th}}$ ac grid, $\text{SoG}_{\Delta,i}$ is equivalently defined as in (4), $V^*_{\text{dc}}$ and $f^*_{\text{ac}}$ representing the nominal reference values for dc voltage and ac frequency, respectively. This definition enables the formulation of grid codes that can naturally be used for both dc and ac microgrids. Both $\text{SoG}_{\text{dc},i}$ and $\text{SoG}_{\text{ac},i}$ are calculated using local measurements obtained from the IC. This allows each converter to independently determine these values without the need for communication. The proposed approach is based on the difference between the dc side SoG ($\text{SoG}_{\text{dc},i}$) and the ac side SoG ($\text{SoG}_{\text{ac},j}$). To suppress inefficient low-power operation and eliminate chatter around the steady state, a symmetric dead-band-implemented with a narrow hysteresis in hardware-is applied

$$P^*_{ij} = \begin{cases} \frac{P^{\max}_{\text{VSC}}}{\sigma} \cdot (\text{SoG}_{\text{dc},i} - \text{SoG}_{\text{ac},j}), & \text{if } |P^*_{ij}| \geq P^{\min}_{\text{VSC}} \\ 0, & \text{otherwise} \end{cases} \tag{7}$$

with $P^*_{ij} \in [-P^{\max}_{\text{VSC}}, P^{\max}_{\text{VSC}}]$ being the transferred power from $i^{\text{th}}$ dc microgrid to the $j^{\text{th}}$ ac grid. By using a deadband between $-P^{\min}_{\text{VSC}}$ and $P^{\min}_{\text{VSC}}$, the function $P^*_{ij}$ is illustrated in Fig. 4 for $\text{SoG}^*_{\text{dc},i} = \text{SoG}^*_{\text{ac},j} = 0.5$ and $\sigma = 0.05$.

### C. Primary DC Voltage and VSC Power Control

The reference output voltage $V^*_{\text{C,B}i}$ of the battery unit can be regulated, for example, using a cascaded PI voltage and current controller, as illustrated in Fig. 5. Depending on the underlying voltage controller structure, it is referred as SoG-based droop (P-controlled) or SoG-based PI (PI-controlled). Each integral control term is saturated and enhanced with an anti-windup. The integral term leads to increased oscillations between the batteries, but removes steady state error. By designing an appropriate gain $K_i$ the oscillations can be reduced significantly.

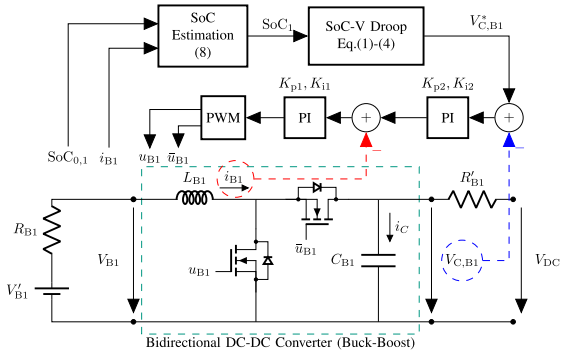


Fig. 5. Proposed control scheme of SoG-based controller with cascaded voltage and current PI and SoC estimation applied to a bidirectional dc–dc converter, operating as boost in one direction (battery discharging) and buck in the other (battery charging).

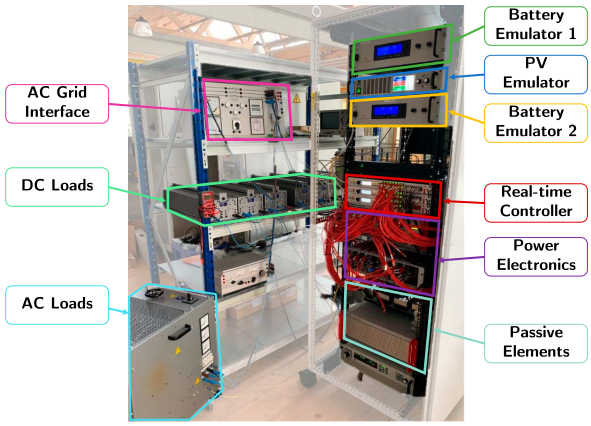


Fig. 6. DC Microgrid experimental setup consisting of PV emulator, loads, real-time controller, SiC-MOSFETs, passive components and battery emulators.

### D. Inherent Tertiary Interface

An inherent tertiary control interface is provided by $\text{SoC}^*_i$, $\text{SoG}^*_{\text{dc}}$, and $\text{SoG}^*_{\text{ac}}$. Adjusting these values allows shifting of operating points, thereby influencing power and energy flows. While these adjustments typically require tertiary control and communication, the primary functionality of the approach remains independent of communication and would continue operating even if communication were to fail.

## III. Experimental Setup of the Microgrid

The experimental results are obtained from a dc microgrid experimental setup as depicted in Fig. 6 [29]. The representative electrical equivalent circuit of the dc microgrid is shown in Fig. 7. The laboratory setup includes two BESS emulators, a PV emulator, passive loads and converter realized by Silicon Carbide (SiC)-MOSFETs. The switching frequency is chosen to be 20 kHz. The IC is limited to 15 kW. The microgrid parameters corresponding to Fig. 7 are listed in Table II. Due to identical hardware across all converters, the values in Table II

This article has been accepted for inclusion in a future issue of this journal. Content is final as presented, with the exception of pagination.



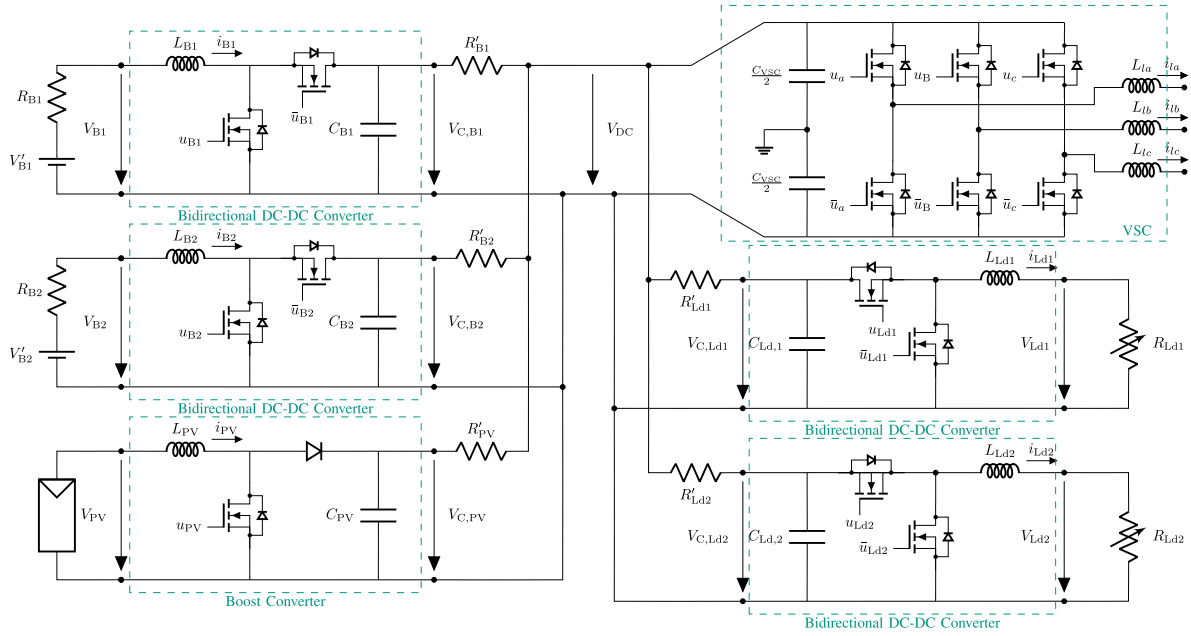


Fig. 7. Electrical circuit of the considered dc microgrid setup.

TABLE II
CIRCUIT PARAMETERS OF THE EXPERIMENTAL MICROGRID SETUP

| Battery 1 | Battery 2 | PV | Load 1 | Load 2 | Value |
|---|---|---|---|---|---|
| $R_{\mathrm{B1}}$ | $R_{\mathrm{B2}}$ | $R_{\mathrm{PV}}$ | $R_{L,Ld1}$ | $R_{L,Ld2}$ | 0.1 Ω |
| $C_{\mathrm{B1}}$ | $C_{\mathrm{B2}}$ | $C_{\mathrm{PV}}$ | $C_{L,Ld1}$ | $C_{L,Ld2}$ | 500 μF |
| $R'_{\mathrm{B1}}$ | $R'_{\mathrm{B2}}$ | $R'_{\mathrm{PV}}$ | $R'_{\mathrm{Ld1}}$ | $R'_{\mathrm{Ld2}}$ | 0.1 Ω |
| $L_{\mathrm{B1}}$ | $L_{\mathrm{B2}}$ | $L_{\mathrm{PV}}$ | $L_{\mathrm{Ld1}}$ | $L_{\mathrm{Ld2}}$ | 2.5 mH |

are likewise uniform across components and are listed in the last column for each row. The IC's dc side is designated as the point of common coupling.

### A. Battery Energy Storages

The SoC estimation is based on the coulomb counting method [30]

$$\mathrm{SoC}_i(t) = \mathrm{SoC}_{0,i} - \frac{1}{C_i}\int_{t_0}^{t} i_{\mathrm{B}i}(\tau)\,d\tau \quad \text{for} \quad t \geq t_0 \qquad (8)$$

where $\mathrm{SoC}_{0,i}$ is the initial SoC, $C_i$ is the capacity (in Ah) and $i_{\mathrm{B}i}$ is the current of the $i^{\mathrm{th}}$ battery. Ageing effects or temperature influences are not considered in this article. The BESSs are emulated by a bidirectional power amplifier with $P_{\max} = 7.5\,\mathrm{kW}$. The nominal voltages are $V_{\mathrm{B1}} = V_{\mathrm{B2}} = 380\,\mathrm{V}$ and the initial values of SoC are chosen as $\mathrm{SoC}_1 = 0.6$ and $\mathrm{SoC}_2 = 0.4$.

### B. Renewable Energy Sources

The approach presented is applicable to microgrids with different RES. Due to the significant expansion of photovoltaics, this work considers it as the primary generation within the grid. The PV panels arranged in a string structure are considered as the main generation of RES in the dc microgrid. By using an incremental conductance algorithm [31], [32], the Maximum Power Point (MPP) is tracked. Through the SoG concept, the curtailment of PV systems can also be integrated locally into the MPPT algorithm, based on the voltage measurement and the SoG derived from it, as this allows inference about the SoC of the batteries.

### C. Variable Load Systems

The loads are resistive loads. While resistive loads may not accurately represent the dynamics of all real-world loads, they serve as a reliable and controllable means of testing the stability and performance of the SoG-based control. The primary voltage and current regulators are assumed to function adequately. The load power can be increased or decreased between 0 and 5.0 kW by adjusting the resistor's corresponding ohmic value. The loads are split into two different voltage levels. Devices with a smaller power consumption are connected to a 120 V bus, while larger loads are considered to be connected to a 230 V bus.

### D. AC Grid Connection

The dc–ac interlink is a VSC, highlighted in Fig. 7, controlled in grid following mode. Each semiconductor of the VSC converter has internal resistances $R_{06} = R_{07} = R_{08} = 10\,\mathrm{m\Omega}$ representing the semiconductor losses. The capacitors of the VSC are $C_{\mathrm{VSC}} = 1.5\,\mathrm{mF}$ and the inductors $L_{la} = L_{lb} = L_{lc} = 2.5\,\mathrm{mH}$. The nominal power is $P_{\mathrm{VSC}}^{\max} = 15\,\mathrm{kW}$. For the demonstration of the functionality of the presented approach, frequency transitions are required, thus an emulator is employed for the ac grid side.

## IV. System Stability Analysis

In this section, we demonstrate the small-signal stability of the proposed control method using Lyapunov's indirect method

This article has been accepted for inclusion in a future issue of this journal. Content is final as presented, with the exception of pagination.



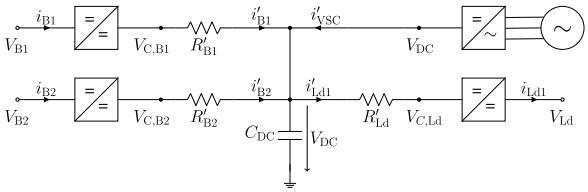


Fig. 8. Simplified equivalent circuit diagram of a dc microgrid.

[33]. An equivalent microgrid model is developed to facilitate this analysis, incorporating two batteries, an output current $i_{\mathrm{Ld}}$ representing the combined load and PV-generated currents, and an ac connection, as illustrated in Fig. 8.

To simplify the stability analysis, we assume the following hierarchy of dynamic responses based on their characteristic timescales: 1) The current dynamics are faster than the voltage dynamics; and 2) the voltage dynamics of the batteries are faster than the SoC dynamics. This hierarchy leverages time scale separation principles, where the current, voltage, and SoC dynamics are categorized as fast, medium, and slow, respectively. This approach aligns with singular perturbation theory, which allows the model to be simplified by approximating the current loop as an algebraic gain during the voltage regulator design [34]. This simplification enables a more tractable analysis focused on the slower voltage and SoC dynamics, as represented in the system's state-space form

$$\dot{x} = \Phi(x) = \begin{bmatrix} \dot{V}_{\mathrm{dc}} \\ \dot{\mathrm{SoC}}_1 \\ \dot{\mathrm{SoC}}_2 \end{bmatrix} \tag{9}$$

$$= \begin{bmatrix} \frac{1}{C_{\mathrm{dc}}}\left(\frac{(V_{\mathrm{C,B1}}-V_{\mathrm{dc}})}{R'_{\mathrm{B1}}} + \frac{(V_{\mathrm{C,B2}}-V_{\mathrm{dc}})}{R'_{\mathrm{B2}}} - i'_{\mathrm{Ld}} + I_{\mathrm{VSC}}\right) \\ -\frac{1}{C_1}\left(\frac{1}{R'_{\mathrm{B1}}}\left(V^*_{\mathrm{dc}}\left(1+\sigma\frac{\mathrm{SoC}_1-\mathrm{SoC}^*_1}{\mathrm{SoC}_{\Delta 1}}\right)-V_{\mathrm{dc}}\right)\frac{V_{\mathrm{C,B1}}}{V_{\mathrm{B1}}}\right) \\ -\frac{1}{C_2}\left(\frac{1}{R'_{\mathrm{B2}}}\left(V^*_{\mathrm{dc}}\left(1+\sigma\frac{\mathrm{SoC}_2-\mathrm{SoC}^*_2}{\mathrm{SoC}_{\Delta 2}}\right)-V_{\mathrm{dc}}\right)\frac{V_{\mathrm{C,B2}}}{V_{\mathrm{B2}}}\right) \end{bmatrix}$$

where $V_{\mathrm{C,B1}}$ and $V_{\mathrm{C,B2}}$ are defined as in (1) and the VSC current is given by

$$I_{\mathrm{VSC}} = \frac{P^{\max}_{\mathrm{VSC}}}{\sigma V_{\mathrm{dc}}}\left(\mathrm{SoG}_{\mathrm{dc}} - \mathrm{SoG}_{\mathrm{ac}}\right) \tag{10}$$

where $\mathrm{SoG}_{\mathrm{dc}}$ and $\mathrm{SoG}_{\mathrm{ac}}$ are defined as in (5) and (6), respectively, and $I_{\mathrm{VSC}}$ is derived from (7).

Setting $\dot{x} = 0$ leads to the unique equilibrium point

$$x^* = \begin{bmatrix} V^*_{\mathrm{dc}} \\ \mathrm{SoC}^*_1 \\ \mathrm{SoC}^*_2 \end{bmatrix}. \tag{11}$$

For the linearization around $x^*$ the Jacobian $J$ is derived as

$$J = \frac{\partial \Phi(x)}{\partial x} = \begin{bmatrix} \frac{\partial \Phi_1}{\partial V_{\mathrm{dc}}} & \frac{\partial \Phi_1}{\partial \mathrm{SoC}_1} & \frac{\partial \Phi_1}{\partial \mathrm{SoC}_2} \\ \frac{\partial \Phi_2}{\partial V_{\mathrm{dc}}} & \frac{\partial \Phi_2}{\partial \mathrm{SoC}_1} & 0 \\ \frac{\partial \Phi_3}{\partial V_{\mathrm{dc}}} & 0 & \frac{\partial \Phi_3}{\partial \mathrm{SoC}_2} \end{bmatrix}\Bigg|_{x=x^*} \tag{12}$$

where each partial derivative is defined as

$$\frac{\partial \Phi_1}{\partial V_{\mathrm{dc}}} = -\frac{1}{C_{\mathrm{dc}}}\left(\frac{1}{R'_{\mathrm{B1}}} + \frac{1}{R'_{\mathrm{B2}}} - \frac{\partial I_{\mathrm{VSC}}}{\partial V_{\mathrm{dc}}}\right)$$

$$\frac{\partial \Phi_1}{\partial \mathrm{SoC}_1} = \frac{1}{C_{\mathrm{dc}}R'_{\mathrm{B1}}} \cdot \frac{\partial V_{\mathrm{C,B1}}}{\partial \mathrm{SoC}_1}$$

$$\frac{\partial \Phi_1}{\partial \mathrm{SoC}_2} = \frac{1}{C_{\mathrm{dc}}R'_{\mathrm{B2}}} \cdot \frac{\partial V_{\mathrm{C,B2}}}{\partial \mathrm{SoC}_2}$$

$$\frac{\partial \Phi_2}{\partial V_{\mathrm{dc}}} = \frac{1}{C_1 R'_{\mathrm{B1}}} \cdot \frac{V_{\mathrm{C,B1}}}{V_{\mathrm{B1}}}$$

$$\frac{\partial \Phi_2}{\partial \mathrm{SoC}_1} = -\frac{\sigma {V^*_{\mathrm{dc}}}^2}{C_1 R'_{\mathrm{B1}} \mathrm{SoC}_{\Delta 1} V_{\mathrm{B1}}}$$

$$\frac{\partial \Phi_3}{\partial V_{\mathrm{dc}}} = \frac{1}{C_2 R'_{\mathrm{B2}}} \cdot \frac{V_{\mathrm{C,B2}}}{V_{\mathrm{B2}}}$$

$$\frac{\partial \Phi_3}{\partial \mathrm{SoC}_2} = -\frac{\sigma {V^*_{\mathrm{dc}}}^2}{C_2 R'_{\mathrm{B2}} \mathrm{SoC}_{\Delta 2} V_{\mathrm{B2}}}.$$

Setting the parameters $V^*_{\mathrm{dc}} = 700\,\mathrm{V}$, $f^*_{\mathrm{ac}} = 50\,\mathrm{Hz}$, $\mathrm{SoC}^*_1 = 0.5$, $\mathrm{SoC}^*_2 = 0.5$, $\mathrm{SoC}_{\Delta 1} = 0.5$, $\mathrm{SoC}_{\Delta 2} = 0.5$, $\mathrm{SoC}_{\Delta \mathrm{VSC}} = 0.5$, $P^{\max}_{\mathrm{VSC}} = 5\,\mathrm{kW}$, $C_{\mathrm{dc}} = 0.3 \times 10^{-3}$ F, $R'_{\mathrm{B1}} = R'_{\mathrm{B2}} = 0.1\,\Omega$, $C_1 = C_2 = 100$ Ah, $V_{\mathrm{B1}} = V_{\mathrm{B2}} = 380$ V, and $\sigma = 0.05$, the resulting eigenvalues are

$$\lambda_1 = -4.83 \times 10^6, \quad \lambda_2 = -1.2716, \quad \lambda_3 = -1.2894.$$

Following the eigenvalue sensitivity analysis, variations in the parameters $R'_{\mathrm{B1}}$ and $R'_{\mathrm{B2}}$ between 0.1 and 5 $\Omega$, as well as $C_1$ and $C_2$ between 1 and 10 A h, result in pole shifts towards the imaginary axis; however, the poles remain in the stable left half-plane, preserving stability. Specifically, the dominant poles' movements under changes in $R'_{\mathrm{B1}}$ and $R'_{\mathrm{B2}}$ are depicted in Fig. 9(a), while the effects of changes in $C_1$ and $C_2$ are shown in Fig. 9(b). In contrast, variations in $C_{\mathrm{dc}}$ primarily impact the nondominant pole $\lambda_1$, which lies far left in the complex plane, thereby exerting minimal influence on system stability. In addition, the sensitivity of the system's eigenvalues with respect to the control parameter $\sigma$ is examined in Fig. 9(c). The parameter $\sigma$ governs the steepness of the SoC-to-voltage projection and thereby influences the strength of the balancing action. For small values up to $\sigma = 0.04$, the dominant eigenvalue remains approximately constant at $\lambda = -0.214$, indicating robust damping. However, as $\sigma$ increases beyond this point, the poles progressively move toward the imaginary axis, reflecting a reduction in system damping and slower convergence dynamics. Despite this, all poles remain in the left-half complex plane, confirming that small-signal stability is preserved for $\sigma \leq 0.25$. This behavior highlights a critical trade-off in the controller design: while higher values of $\sigma$ improve the responsiveness of the SoC balancing mechanism, they also reduce the system's robustness margin. Therefore, the mapping gain must be carefully tuned to ensure stable operation without compromising dynamic performance. These eigenvalue distributions validate small-signal stability, as all poles retain negative real parts, demonstrating that the proposed dc microgrid control strategy reliably stabilizes the system around its equilibrium point $x^*$. While no instability is observed within the considered parameter ranges, it is important to note the limits of applicability. Instability may occur if feeder resistances become excessively large [Fig. 9(a)], if the mapping gain $\sigma$ is chosen disproportionally high [Fig. 9(c)], or if the assumed time-scale separation between current, voltage, and SoC dynamics is violated.

This article has been accepted for inclusion in a future issue of this journal. Content is final as presented, with the exception of pagination.



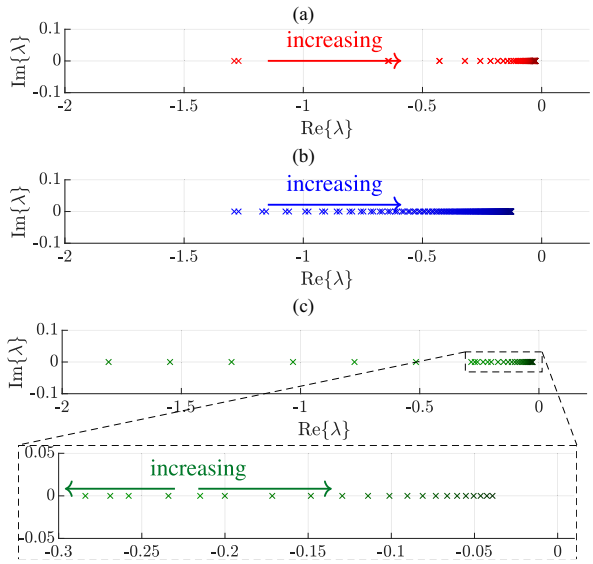


Fig. 9. Pole analysis illustrating the dominant poles for (a) variations in $R'_{B1}$ and $R'_{B2}$ between 0.1 and 5 Ω; (b) similar effects from changes in $C_1$ and $C_2$ between 1 and 10 a h; and (c) influence of control parameter $\sigma$ varied between 0 and 0.25. Increasing values of $\sigma$ lead to dominant pole movements towards the imaginary axis, reducing damping.

### A. Robustness Analysis for Frequency Variations

The equilibrium point $x^*$ in (11) is derived under the assumption of a constant ac frequency $f_{ac} = f^*_{ac}$. However, in practical implementations, the frequency $f_{ac}(t)$ may vary due to dynamic disturbances in the ac grid. This variation affects the SoG mapping and consequently the dc side equilibrium, as the VSC current $I_{VSC}$ in (10) depends directly on $f_{ac}(t)$. To analyze this, we recast the nonlinear system in (9) as

$$\dot{\tilde{x}} = f(\tilde{x}) + g(\tilde{x})u(t) \tag{13}$$

where $u(t) := f_{ac} - f^*_{ac}$ and $\tilde{x}(t) := x(t) - x^*$. Furthermore, $g(\tilde{x}) = \begin{bmatrix} g_1(\tilde{x}) & 0 & 0 \end{bmatrix}^\top$ which reflects the fact that frequency deviations influence only the dc voltage dynamics via the interlinking converter. The specific form of $g_1(\tilde{x})$ is derived from (9) and given by

$$g_1(\tilde{x}) = -\frac{P^{\max}_{VSC} \cdot SoC_\Delta}{\sigma^2 V_{dc} f^*_{ac} C_{dc}}. \tag{14}$$

This input-to-state stability (ISS)-based analysis approach is closely aligned with the robust frequency stability analysis presented in [35], and follows the framework provided by [33, Theorem 4.19 and Lemma 9.2]. The input-to-state stability (ISS) of this system is being examined with respect to the time-varying input $u(t)$ implies that, if the system $\dot{x} = \Phi(x, u)$ is ISS, then for any bounded input $u(t)$, the state $x(t)$ remains bounded and is ultimately bounded to a neighborhood around the equilibrium $x^*$ whose radius depends on the magnitude of the input perturbation. To prove ISS, we define the Lyapunov function

$$V(\tilde{x}) = \frac{1}{2}\|\tilde{x}\|^2 \tag{15}$$

TABLE III
POWER STEPS IN EXPERIMENTAL TEST

| | ① | ② | ③ | ④ | ⑤ | ⑥ | ⑦ |
|---|---|---|---|---|---|---|---|
| $P_{PV}$ [kW] | 0.0 | 3.0 | 0.0 | 1.5 | 1.5 | 1.5 | 3.0 |
| $P_{Ld1}$ [kW] | 1.0 | 1.0 | 1.0 | 1.0 | 3.0 | 1.0 | 1.0 |
| $P_{Ld2}$ [kW] | 0.5 | 0.5 | 0.5 | 0.5 | 1.0 | 0.5 | 0.5 |

which satisfies

$$\alpha_1(\|\tilde{x}\|) \le V(\tilde{x}) \le \alpha_2(\|\tilde{x}\|), \quad \alpha_1(r) = \alpha_2(r) = \frac{1}{2}r^2$$

with $\alpha_1$,$\alpha_2$ being class $\mathcal{K}_\infty$ functions. Taking the time derivative of $V(\tilde{x})$ along system trajectories leads to

$$\dot{V}(\tilde{x}, u) = \underbrace{(\tilde{x})^T f((\tilde{x})}_{\text{stabilizing}} + \underbrace{(\tilde{x})^T g(\tilde{x})u}_{\text{disturbing}}. \tag{16}$$

Based on the linearized stability analysis in Section IV, the autonomous part $\dot{x} = f(x)$ is locally exponentially stable. Therefore, there exists a constant $\lambda > 0$ such that

$$\tilde{x}^T f(x) \le -\lambda\|\tilde{x}\|^2.$$

The disturbance term satisfies

$$\tilde{x}^\top g(\tilde{x})u \le \|\tilde{x}\| \cdot \|g(\tilde{x})\| \cdot |u|. \tag{17}$$

Hence

$$\dot{V}(x, u) \le -\lambda\|\tilde{x}\|^2 + \|\tilde{x}\| \cdot \|g(\tilde{x})\| \cdot |u|.$$

Now, if

$$\|\tilde{x}\| \ge \rho(|u|) := \frac{\|g(\tilde{x})\|}{\lambda}|u| \tag{18}$$

then

$$\dot{V}(x, u) \le -W_3(x), \quad W_3(x) := \lambda\|\tilde{x}\|^2$$

where $W_3(x)$ is positive definite. This verifies the conditions of Theorem 4.19 [33], confirming that the system is ISS. Hence, there exists a class $\mathcal{KL}$ function $\beta$ and a class $\mathcal{K}$ function $\gamma$ such that

$$\|\tilde{x}\| \le \beta(\|x(0) - x^*\|, t) + \gamma\left(\sup_{0\le\tau\le t}|u(\tau)|\right) \tag{19}$$

with $\gamma = \alpha_1^{-1} \circ \alpha_2 \circ \rho$. From (14) and (18), the maximum frequency deviation that ensures a bounded state deviation $\|\tilde{x}(t)\| \le \varepsilon$ is given by

$$\sup_{0\le\tau\le t}|f_{ac}(\tau) - f^*_{ac}| \le \frac{\lambda\sigma^2 V_{dc} f^*_{ac} C_{dc}}{P^{\max}_{VSC} \cdot SoC_\Delta} \cdot \sqrt{2\varepsilon}. \tag{20}$$

The analysis in this section considers a single IC between the dc and ac subsystems. The extension to multiple ICs requires a multi-input treatment and is outside the scope of this work.

This article has been accepted for inclusion in a future issue of this journal. Content is final as presented, with the exception of pagination.



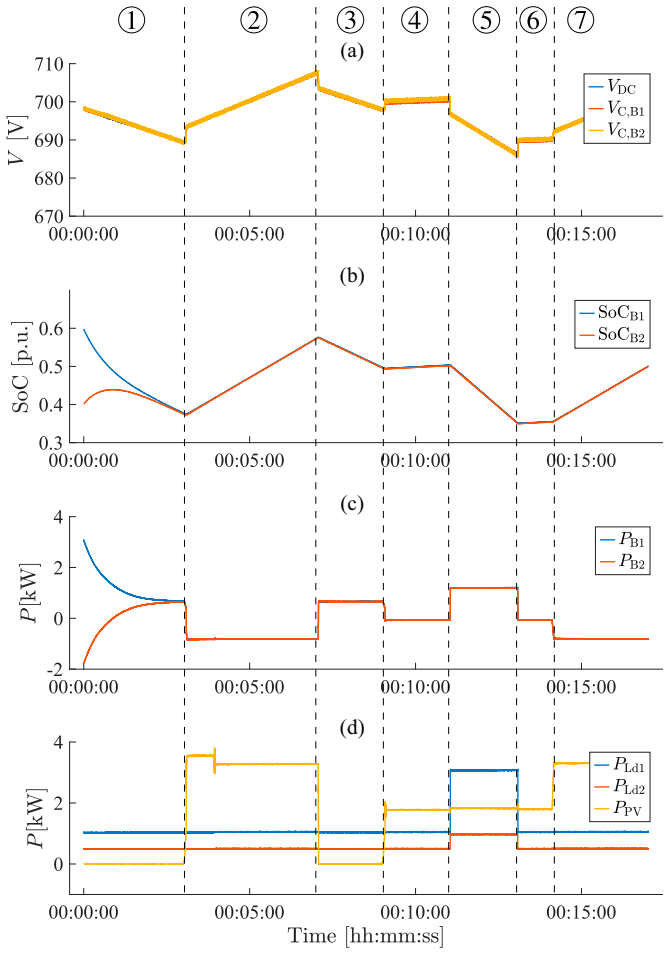


Fig. 10. Experimental results of the proposed SoG-based droop control approach for dc microgrids in islanded mode with two identical batteries. The figure subplots depict: (a) voltage profile of the dc bus; (b) SoCs of the BESSs; (c) battery power variations; and (d) power profiles of the load and PV systems, respectively.

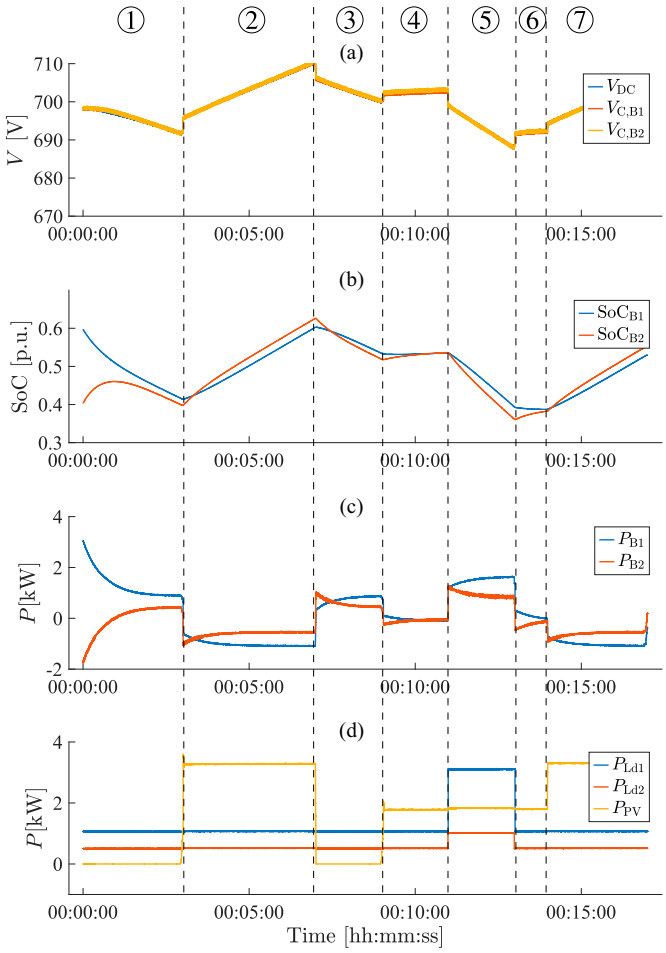


Fig. 11. Experimental results of the proposed SoG-based droop control approach for dc microgrids in islanded mode with two different batteries. The figure subplots depict: (a) voltage profile of the dc bus; (b) SoCs of the BESSs; (c) battery power variations; and (d) power profiles of the load and PV systems, respectively.

## V. Experimental Validation

The results in this section demonstrate the effectiveness of the proposed SoG-based control approach for dc microgrids, validated across multiple scenarios. All underlying data and code to reproduce the results are archived at [36]. In Case I, the dc microgrid operates in islanded mode with two identical batteries. Case II examines the impact of using two different batteries and line resistances, comparing both the droop-based and PI-based methods. Finally, Case III investigates the ac-coupled mode with two identical batteries on the dc side. The values of $\mathrm{SoC}_1^*$, $\mathrm{SoC}_2^*$, and $\mathrm{SoG}_{\mathrm{dc1}}^* = \mathrm{SoG}_{\mathrm{ac1}}^*$ are all set to 0.5. The experimental steps are listed in Table III, where $P_{\mathrm{PV}}$ represents the PV output power, and $P_{\mathrm{Ld1}}$ and $P_{\mathrm{Ld2}}$ denote the power consumed by load 1 and load 2, respectively. Three distinct PV transitions are imposed using the programmable PV emulator: a sharp increase from 0 kW to 3 kW in Step ②, an abrupt drop back to 0 kW in Step ③, and two moderate increases to 1.5 kW in Steps ④ and ⑦. These PV steps are designed to emulate realistic fluctuations in renewable generation and to test the controller's robustness against rapid injection changes. In parallel, the loads $P_{\mathrm{Ld1}}$ and $P_{\mathrm{Ld2}}$ are varied across the test sequence, with Step ⑤ introducing a temporary load increase from 1.5 kW to 4.0 kW total. These combined variations challenge the system to maintain dc voltage regulation, SoC balancing, and power-sharing under non-steady operating conditions. Within the test sections, minor variations in PV power injection may occur due to changes in the MPPT tracker's operating point. However, these fluctuations are insignificant for the experiment and therefore negligible.

### A. Case I (SoG-Based Droop With Identical Batteries)

The experimental validation of this approach is conducted by variations in the PV power, and changes in load. To achieve significant results within a reasonable timeframe, the usable energy of each battery is set to a small value ($C_1 = C_2 = 0.8$ Ah), without compromising result accuracy. This choice does not limit the applicability to larger battery capacities.

The results in Fig. 10 demonstrate the effectiveness of the proposed SoG-based droop control approach for dc microgrids.

This article has been accepted for inclusion in a future issue of this journal. Content is final as presented, with the exception of pagination.



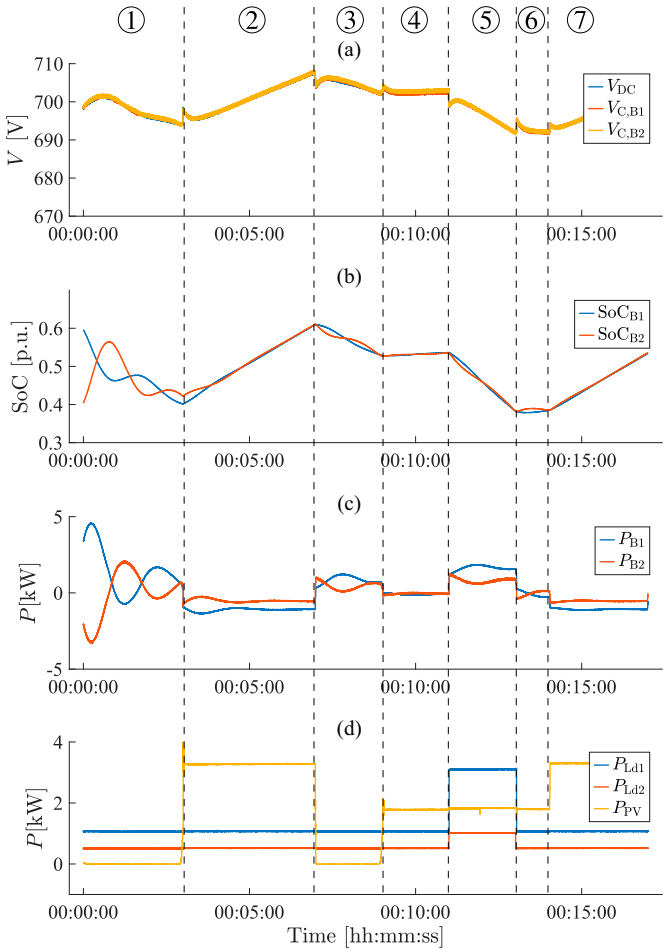


Fig. 12. Experimental results of the proposed SoG-based PI control approach for dc microgrids in islanded mode with two different batteries. The figure subplots depict: (a) voltage profile of the dc bus; (b) SoCs of the BESSs; (c) battery power variations; and (d) power profiles of the load and PV systems, respectively.

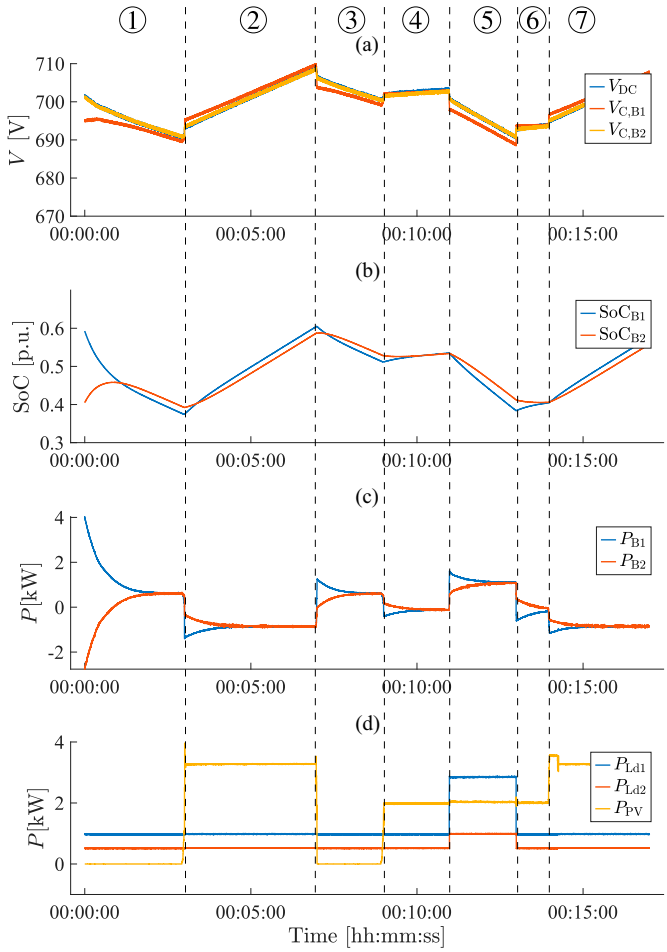


Fig. 13. Experimental results of the proposed SoG-based droop control approach for dc microgrids in islanded mode with different line resistances of the batteries. The figure subplots depict: (a) voltage profile of the dc bus; (b) SoCs of the BESSs; (c) battery power variations; and (d) power profiles of the load and PV systems, respectively.

First, the dc bus voltage $V_{\mathrm{dc},i}$ remains stable at the determined voltage throughout the experiments, with minor fluctuations in response to load variations and renewable energy inputs, demonstrating effective regulation within the desired range for stable microgrid operation. Second, the SoC trajectories of individual BESS units indicate successful SoC balancing, as each unit gradually converges to a similar SoC level, achieved by the SoG-based control strategy. Furthermore, both batteries demonstrate effective power-sharing, dynamically adjusting power output based on load demand and renewable energy availability.

### *B. Case II (SoG-Based Control With Different Batteries and Line Resistances)*

The variations in input and load used to investigate the SoG-based approach with different batteries are the same as in Case I and are listed in Table III. In this case, Battery 2 has half the capacity of Battery 1 ($C_1 = 1.0\,\mathrm{Ah}$ and $C_2 = 0.5\,\mathrm{Ah}$). The results for the droop-based SoG control are shown in Fig. 11. Compared with the results with two identical batteries shown in Fig. 10, we observe a divergence of the SoG depending on the load conditions. However, when employing a SoG-based PI approach, the differences between the two SoCs are mitigated by the integral component, as depicted in Fig. 12, without any adaptions on the droop coefficients. Nevertheless, the drawback of the PI-based method is that it leads to energy oscillations between the batteries during ① and ③. For different battery capacities, the integral component introduces a trade-off between SoC equalization accuracy and power oscillations. Additionally, the impact of line resistances on performance is investigated. For this analysis, the line resistance $R'_{\mathrm{B1}}$ is increased to 2.5 Ω, corresponding to a line length of 375 m with a copper cable cross-section of 2.5 $\mathrm{mm}^2$. The results are presented in Fig. 13 for SoG droop based-control. It can be observed that the SoC balancing capability is affected; however, unlike conventional droop control, the power balancing capability is maintained. In the scenario involving different line resistances, the inclusion of the integral component does not enhance the accuracy of SoC equalization, unlike its impact in the case of two distinct batteries.

This article has been accepted for inclusion in a future issue of this journal. Content is final as presented, with the exception of pagination.



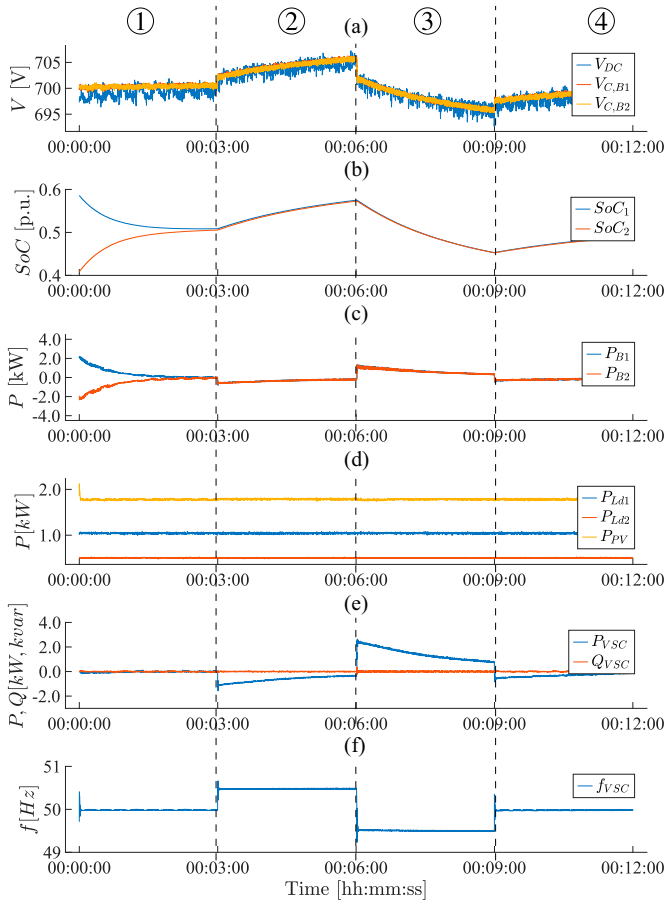


Fig. 14. Experimental results of the proposed SoG-based droop control approach for ac-coupled dc microgrids. The figure subplots depict: (a) voltage profile of the dc bus; (b) SoCs of the BESSs; (c) battery power variations; (d) power profiles of the load and PV systems; (e) active and reactive power of the VSC; and (f) ac grid frequency, respectively.

TABLE IV
FREQUENCY STEPS IN AC-COUPLED TEST SCENARIO

| | ① | ② | ③ | ④ |
|---|---|---|---|---|
| $f_{\text{ac}}$ [Hz] | 50.0 | 50.5 | 49.5 | 50.0 |

### C. Case III (AC-Coupled SoG-Based Control)

The results shown in Fig. 14 demonstrate the effectiveness of the proposed SoG-based control approach for ac-coupled dc microgrids. While the dc side operates similarly to that discussed in the previous section, this section focuses on insights related to the ac interlink. The VSC dynamically adjusts its active power $P_{\text{VSC}}$ to regulate power flow between the ac and dc side. Reactive power provision is not considered, and the reactive power reference is set to $Q^*_{\text{VSC}} = 0$. The test sequence includes four distinct frequency steps on the ac side, as summarized in Table IV.

During ①, the ac grid frequency $f$ is set to 50 Hz with $\text{SoG}_{\text{dc},i}$ and $\text{SoG}_{\text{ac},j}$ both around 0.5, resulting in zero power transfer from the VSC. At step ②, the ac frequency increases to 50.5 Hz, corresponding to $\text{SoG}_{\text{ac},j} = 0.6$, which facilitates power transfer from the ac side to the dc side. As the $\text{SoC}s$ of the batteries rise, leading to an increase in $\text{SoG}_{\text{dc},i}$, the VSC power output gradually decreases. The opposite effect occurs in ③, where power flow reverses due to a change in frequency. Finally, in ④, the frequency is reset to 50 Hz bringing $\text{SoG}_{\text{dc},i}$ back to 0.5. Through dynamic adjustments in active power exchange based on SoG values, the proposed control approach enables the VSC to maintain grid stability.

## VI. CONCLUSION

The present work introduces a novel SoG-based control approach for dc microgrids, providing a communication-free solution for SoC balancing and seamless ac coupling. The proposed control method effectively manages power flow and balances the SoC among ESS units in the dc microgrid without requiring direct communication, addressing a key challenge in decentralized microgrid management. By dynamically adjusting power exchange between the ac and dc sides based on SoG values, the method achieves robust stability and reliable operation under varying load conditions, input power fluctuations, and ac-side frequency deviations. The flexibility of the proposed control approach is further enhanced by inherent tertiary control interfaces, which allow for supervisory adjustments to optimize ESS performance as needed. While additional communication could facilitate more precise adjustments at the tertiary control level, the core method remains fully functional and effective without communication, maintaining its decentralized nature. The SoG-based control method performs effectively in small-scale systems but exhibits sensitivity to line resistances. Stability analysis and experimental results indicate that longer line distances can reduce the precision of SoC balancing and lead to voltage drops, which may destabilize the system. This sensitivity suggests that system configurations with significant line resistances require consideration of potential voltage regulation measures to ensure consistent performance. Comprehensive experimental validations have confirmed the effectiveness of the proposed SoG-based control approach. The results demonstrate not only successful SoC balancing but also stable power regulation, making this method suitable for practical deployment in small-scale dc microgrids, such as residential or islanded systems. Overall, the proposed SoG-based control approach advances dc microgrid control, offering a practical and scalable solution that minimizes communication requirements while ensuring stability and optimal ESS operation.

## REFERENCES

[1] F. Perez and G. Damm, *DC MicroGrids*, Cham, Switzerland: Springer Int. Publ., 2019.
[2] A. Sauer, *The DC-Factory*, Munich, Germany: Hanser eLibrary., 2021.
[3] V. F. Pires A. Pires, and A. Cordeiro, "DC microgrids: Benefits, architectures, perspectives and challenges," *Energies*, vol. 16, no. 3, 2023, Art. no. 1217, doi: 10.3390/en16031217.
[4] M. S. Alam et al., "Renewable energy integration with DC microgrids: Challenges and opportunities," *Electr. Power Syst. Res.*, vol. 234, 2024, Art. no. 110548.

This article has been accepted for inclusion in a future issue of this journal. Content is final as presented, with the exception of pagination.



[5] "IEEE Standard for Interconnection and Interoperability of Distributed Energy Resources with Associated Electric Power Systems Interfaces," *IEEE Std.*, pp. 1547–2018, 2018, doi: 10.1109/IEEESTD.2018.8332112.
[6] C. Jin, P. Wang, J. Xiao, Y. Tang, and F. H. Choo, "Implementation of hierarchical control in DC microgrids," *IEEE Trans. Ind. Electron.*, vol. 61, no. 8, pp. 4032–4042, Aug. 2014.
[7] A. Iovine, T. Rigaut, G. Damm, E. De Santis, and M. D. Di Benedetto, "Power management for a DC microgrid integrating renewables and storages," *Control Eng. Pract.*, vol. 85, pp. 59–79, 2019, doi: 10.1016/j.conengprac.2019.01.009.
[8] R. Bhosale, R. Gupta, and V. Agarwal, "A novel control strategy to achieve SOC balancing for batteries in a DC microgrid without droop control," *IEEE Trans. Ind. Appl.*, vol. 57, no. 4, pp. 4196–4206, Jul./Aug. 2021.
[9] T. A. Fagundes et al., "Battery energy storage systems in microgrids: A review of SoC balancing and perspectives," *IEEE Open J. Ind. Electron. Soc.*, vol. 5, pp. 961–992, 2024.
[10] J. M. Guerrero, J. C. Vasquez, J. Matas, L. G. de Vicuna, and M. Castilla, "Hierarchical control of droop-controlled AC and DC microgrids—A general approach toward standardization," *IEEE Trans. Ind. Electron.*, vol. 58, no. 1, pp. 158–172, Jan. 2011.
[11] E. Kabalci and Y. Kabalci, *Smart Grids and Their Communication Systems*, Singapore: Springer, 2019.
[12] B. Fan et al., "A novel droop control strategy of reactive power sharing based on adaptive virtual impedance in microgrids," *IEEE Trans. Ind. Electron.*, vol. 69, no. 11, pp. 11335–11347, Nov. 2022.
[13] S. Ferahtia, A. Djerioui, H. Rezk, A. Chouder, A. Houari, and M. Machmoum, "Adaptive droop-based control strategy for DC microgrid including multiple batteries energy storage systems," *J. Energy Storage*, vol. 48, 2022, Art. no. 103983.
[14] K. Wang, J. Zhang, X. Qiu, J. Wang, and C. Wang, "Accurate current sharing with SoC balancing in DC microgrid," *Electr. Power Syst. Res.*, vol. 232, 2024, Art. no. 110386.
[15] R. Iqbal, Y. Liu, Y. Zeng, Q. Zhang, and H. Yu, "Adaptive droop-based SoC balancing control scheme for parallel battery storage system in shipboard DC microgrid," *J. Energy Storage*, vol. 79, 2024, Art. no. 110205.
[16] X. Lu, K. Sun, J. M. Guerrero, J. C. Vasquez, and L. Huang, "State-of-charge balance using adaptive droop control for distributed energy storage systems in DC microgrid applications," *IEEE Trans. Ind. Electron.*, vol. 61, no. 6, pp. 2804–2815, Jun. 2014.
[17] X. Lu, K. Sun, J. Guerrero, J. C. Vasquez, and L. Huang, "Double-quadrant SOC-based droop control method for distributed energy storage systems in autonomous DC microgrids," *IEEE Trans. Smart Grid*, vol. 6, no. 1, pp. 147–157, Jan. 2015.
[18] E. K. Belal, D. M. Yehia, and A. M. Azmy, "Adaptive droop control for balancing SOC of distributed batteries in DC microgrids," *IET Gener., Transm. Distrib.*, vol. 13, no. 20, pp. 4667–4676, 2019.
[19] Y. Xia, M. Yu, P. Yang, Y. Peng, and W. Wei, "Generation-storage coordination for islanded DC microgrids dominated by PV generators," *IEEE Trans. Energy Convers.*, vol. 34, no. 1, pp. 130–138, Mar. 2019.
[20] N. Hou and Y. Li, "Communication-free power management strategy for the multiple DAB-based energy storage system in islanded DC microgrid," *IEEE Trans. Power Electron.*, vol. 36, no. 4, pp. 4828–4838, Apr. 2021.
[21] K. D. Hoang and H.-H. Lee, "Accurate power sharing with balanced battery state of charge in distributed DC microgrid," *IEEE Trans. Ind. Electron.*, vol. 66, no. 3, pp. 1883–1893, Mar. 2019.
[22] P. C. Loh, D. Li, Y. K. Chai, and F. Blaabjerg, "Autonomous operation of hybrid microgrid with AC and DC subgrids," *IEEE Trans. Power Electron.*, vol. 28, no. 5, pp. 2214–2223, May 2013.
[23] P. C. Loh, D. Li, Y. K. Chai, and F. Blaabjerg, "Hybrid AC-DC microgrids with energy storages and progressive energy flow tuning," *IEEE Trans. Power Electron.*, vol. 28, no. 4, pp. 1533–1543, Apr. 2013.
[24] N. Eghtedarpour and E. Farjah, "Power control and management in a hybrid AC/DC microgrid," *IEEE Trans. Smart Grid*, vol. 5, no. 3, pp. 1494–1505, May 2014.
[25] C. Weng and Y. Peng, "Adaptive and decentralized SoC-based energy management for grid-connected DC microgrid," in *Proc. 49th Annu. Conf. IEEE Ind. Electron. Soc. (IECON)*, 2023, doi: 10.1109/IECON51785.2023.10312604.
[26] M. Nabatirad, R. Razzaghi, and B. Bahrani, "Decentralized voltage regulation and energy management of integrated DC microgrids into AC power systems," *IEEE J. Emerg. Sel. Topics Power Electron.*, vol. 9, no. 2, pp. 1269–1279, Apr. 2021.
[27] X. Lin, R. Zamora, and C. A. Baguley, "A fully filter-based decentralized control with state of charge balancing strategy for battery energy storage systems in autonomous DC microgrid applications," *IEEE Access*, vol. 9, pp. 15028–15040, 2021, doi: 10.1109/ACCESS.2021.3052924.
[28] J. Su, K. Li, Y. Li, C. Xing, and J. Yu, "A novel SOC-based droop control for battery energy storage systems to support coordinated operation of DC microgrids," *IEEE J. Emerg. Sel. Topics Power Electron.*, vol. 11, no. 1, pp. 312–324, Feb. 2023.
[29] Ö. F. Ekin et al., "The Smart2DC microgrid laboratory at Karlsruhe Institute of Technology," in *Proc. IEEE 7th Int. Conf. DC Microgrids (ICDCM)*, 2025, pp. 1–6, doi: 10.1109/ICDCM63994.2025.11144732.
[30] A. Emami, G. Akbarizadeh, and A. Mahmoudi, "A novel approach for real-time estimation of state of charge in Li-ion battery through hybrid methodology," *IEEE Access*, vol. 12, pp. 148979–148989, 2024.
[31] D. Sera, L. Mathe, T. Kerekes, S. V. Spataru, and R. Teodorescu, "On the perturb-and-observe and incremental conductance MPPT methods for PV systems," *IEEE J. Photovolt.*, vol. 3, no. 3, pp. 1070–1078, Jul. 2013.
[32] D. C. Huynh and M. W. Dunnigan, "Development and comparison of an improved incremental conductance algorithm for tracking the MPP of a solar PV panel," *IEEE Trans. Sustain. Energy*, vol. 7, no. 4, pp. 1421–1429, Oct. 2016.
[33] H. Khalil, Nonlinear control global edition, Pearson Deutschland, 2014. [Online]. Available: https://elibrary.pearson.de/book/99.150005/9781292060699
[34] Y. Ma, D. Zhu, Z. Zhang, X. Zou, J. Hu, and Y. Kang, "Modeling and transient stability analysis for type-3 wind turbines using singular perturbation and Lyapunov methods," *IEEE Trans. Ind. Electron.*, vol. 70, no. 8, pp. 8075–8086, Aug. 2023.
[35] E. Alves, G. Bergna-Diaz, D. Brandao, and E. Tedeschi, "Sufficient conditions for robust frequency stability of AC power systems," *IEEE Trans. Power Syst.*, vol. 36, no. 3, pp. 2684–2692, May 2021.
[36] Ö. Ekin, "Experimental data and scripts for state-of-grid based SoC balancing and AC coupling control for DC microgrids," Sep. 2025, doi: 10.5281/zenodo.17061990.

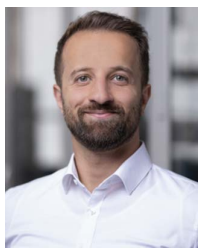

**Ömer Ekin** (Graduate Student Member, IEEE) received the M.Sc. degree in electrical engineering and information technology in 2021 from Karlsruhe Institute of Technology, Karlsruhe, Germany, where he is currently working toward the Ph.D. degree with the Institute for Automation and Applied Informatics.

His research interests include modeling and control of power systems and microgrids.

**Max Leuthaeusser** (Student Member, IEEE) received the B.Eng. degree in electrical engineering from the Dual State University, Mannheim, Germany, in 2016. He is currently working toward the M.Sc. degree in electrical engineering and information technology with the Institute for Automation and Applied Informatics, Karlsruhe Institute of Technology, Karlsruhe, Germany, in 2024.

His research interest includes power system modeling and control.

This article has been accepted for inclusion in a future issue of this journal. Content is final as presented, with the exception of pagination.



**Giovanni De Carne** (Senior Member, IEEE) received the B.Sc. and M.Sc. degrees in electrical engineering from the Polytechnic University of Bari, Bari, Italy, in 2011 and 2013, respectively, and the Ph.D. degree in electrical and information technology from the Chair of Power Electronics, Kiel University, Kiel, Germany, in 2018.

He is currently W3 (Full) Professor with the Institute for Technical Physics, Karlsruhe Institute of Technology, Karlsruhe, Germany, where he leads the "Real Time Systems for Energy Technologies" Group and the "Power Hardware In the Loop Lab". He is currently Supervising Postdoctoral students, managing academic and industrial projects, and developing multi-MW power hardware in the loop testing infrastructures for energy storage systems and hydrogen-based technologies. He has authored/coauthored more than 100 peer-reviewed scientific articles. His research interests include power electronics integration in power systems, solid-state transformers, real-time modelling, and power hardware in the loop.

Dr. De Carne is currently in the IEEE Power Electronics Society AdCom Member-at-Large, he has been the Technical Program Committee Chair for several IEEE conferences, and Associate Editor and Guest Editors of several IEEE Power Electronics Society Journals.

**Veit Hagenmeyer** (Member, IEEE) received his Ph.D. in automation from Université Paris XI, Paris, France.

He is currently a Professor of energy informatics with the Department of Informatics and Director of the Institute for Automation and Applied Informatics with Karlsruhe Institute of Technology (KIT), Karlsruhe, Germany. Before his professorship, he served as power plant director responsible for three power plants and the energy network of BASF with Ludwigshafen site, Germany. He is the spokesperson for the national "Energy System Design" program of Helmholtz Association and the Founding Director of the national BMBF Kopernikus ENSURE project for new grid structures. He also serves as the actual spokesperson of the Energy Lab with KIT and the associated Living Lab Energy Campus project. He is a President of the European Institute for Energy Research and a member of the Scientific Advisory Board of Électricité de France. His research interests include the modeling, optimization, and control of sector-integrated energy systems; machine-learning-based forecasting of uncertain demand and generation in energy systems predominantly driven by renewable energies; and the integrated cybersecurity of such systems.